

Article

Electrochemical properties of transition metal oxide-based nanocomposites for energy storage systems

Amna Khalid¹, Javed Iqbal^{1,*}, Sobia Jabeen¹, Muhammad Awais Qarni², Ming Xiao³, Naeem Ahmad²

- ¹ Department of Physics, Faculty of Natural Sciences, Quaid-I-Azam University, Islamabad 45320, Pakistan
- ² Department of Physics, Faculty of Sciences, International Islamic University, Islamabad 45320, Pakistan
- ³ Department of Microelectronics Science and Technology, School of Microelectronics Science and Technology, Sun Yat-sen University, Zhuhai 510275, China
- * Corresponding author: Javed Iqbal, javed.saggu@qau.edu.pk

CITATION

Khalid A, Iqbal J, Jabeen S et al. (2025). Electrochemical properties of transition metal oxide-based nanocomposites for energy storage systems. Characterization and Application of Nanomaterials. 8(3): 11706.

https://doi.org/10.24294/CAN11706

ARTICLE INFO

Received: 24 April 2025 Accepted: 6 November 2025 Available online: 24 November 2025

COPYRIGHT



Copyright © 2025 by author(s). Characterization and Application of Nanomaterials is published by EnPress Publisher, LLC. This work is licensed under the Creative Commons Attribution (CC BY) license.

https://creativecommons.org/licenses/by/4.0/

Abstract: The rapid growth of portable electronics and electric vehicles has intensified the global demand for high-performance energy storage devices with superior power density, energy density, and long cycle life. Among transition metal oxide-based electrode materials with potential for energy storage, we report the development of MnO₂–V₂O₅ nanocomposite electrodes for supercapacitor applications. Pure MnO_2 and V_2O_5 were successfully fabricated via a simple and economical sol-gel method, while $(MnO_2)x-(V_2O_5)1-x$ (x = 1, 0.75, 0.50, and 0) nanocomposites were fabricated through an ex situ method. Analytical techniques, including X-ray diffraction, scanning electron microscopy, Fourier transform infrared spectroscopy, and UV-visible spectroscopy, were employed to investigate the structural, morphological, and optical properties of the electrodes. Furthermore, the electrochemical properties were systematically analysed using cyclic voltammetry, galvanostatic chargedischarge measurements, and electrochemical impedance spectroscopy. The (MnO2)0.75- $(V_2O_5)0.25$ nanocomposite demonstrated a remarkable specific capacitance of 666 F/g at a current density of 0.5 A/g in 1 M KOH electrolyte. Additionally, the electrode material exhibited an energy density of 23 Wh/kg and a power density of 450 W/kg, while maintaining a capacitance retention of 95% after 1,500 cycles. The incorporation of V₂O₅ boosted the conductivity and significantly optimised the number of lattice defects. This work substantially reinforces the importance of metal oxide-based nanocomposites for future energy storage devices.

Keywords: manganese dioxide; supercapacitor; vanadium pentoxide; electrochemical properties; nanocomposites

1. Introduction

In the modern era, increasing energy demands that primarily rely on nonrenewable fossil fuels present a significant risk to human well-being. To address these challenges, efforts have been directed toward developing renewable, eco-friendly, and economical energy storage devices [1,2]. Renewable energy storage devices are widely utilised in the present era, spanning from portable devices and electric vehicles to large-scale grid storage systems [3]. Although Li-ion batteries are prevalent owing to their high energy density, there is a critical need for innovative materials and designs capable of delivering higher specific capacitance (C_w) and faster charging rates [4,5]. Supercapacitors have recently emerged as a desirable option for various energy storage applications due to their increased power density, rapid charge and discharge rates, and long lifespan [6,7]. Researchers have encountered challenges

in improving the energy density of supercapacitors [8,9], which involves optimising the selection and fabrication of appropriate electrode materials that possess a large surface area, low solution resistance, high chemical stability, and high conductivity [10,11].

Transition metal oxides (TMOs) are prominent pseudocapacitive materials owing to their unique properties, including low cost, abundant oxidation states, reversible surface redox reactions, minimal toxicity, and high theoretical C_w [12]. Pseudocapacitors are based on reversible redox reactions at the electrode surface. This redox process entails ion migration between distinct oxidation states of the electrode material. Charges or ions in pseudocapacitive materials can be stored through mechanisms such as adsorption, intercalation, and surface redox reactions [13–15]. Owing to the synergistic interactions of metal cations, mixed TMOs potentially exhibit superior physical and chemical properties [16], such as improved electrical conductivity and enhanced charge storage capacity in comparison to individual metal oxides [17].

The primary disadvantage of TMOs is their low electrical conductivity. To address this, various studies have aimed to increase the electrical conductivity of TMOs by creating composite materials [18–20]. Extensive research has focused on TMOs, such as ruthenium dioxide (RuO₂) [21], hafnium dioxide (HfO₂) [22], iron(III) oxide (Fe₂O₃) [23,24], vanadium pentoxide (V₂O₅) [25], tungsten trioxide (WO₃) [26], and manganese dioxide (MnO₂) [27], for their application in supercapacitors. The pseudocapacitor electrode material MnO₂ is gaining attention because the single-electron redox process in each manganese (Mn) atom contributes to a relatively large theoretical capacitance of 1,370 F/g. It is affordable, abundant, non-toxic, and has low conductivity [28–30]. Mn exists in a 2D tunnelling structure that facilitates electron transfer, resulting in a relatively high capacitance value, known as α , β , γ , λ , and δ forms, through distinct configurations of MnO₆ octahedra, where the Mn atom is centrally located, surrounded by six oxygen atoms at each corner [31,32].

However, their low conductivity and volume expansion during discharge present significant challenges. To address these issues, numerous studies have been undertaken. Wu et al. [33] examined Fe-doped MnO₂ electrodes, enhancing their C_w to 340 F/g at a current density of 2 A/g. Tatrari et al. [34] compared 3D graphene hydrogel and WO₃–MnO₂ composites, demonstrating their superior performance in asymmetric supercapacitors, with the MnO₂ composite achieving a C_w of 430 F/g at a current density of 1 A/g. Shen et al. [35] presented the synthesis of δ -MnO₂/soybean pod carbon via *in situ* hydrothermal methods, showcasing its high-performance application with a C_w of 380 F/g at a current density of 1 A/g.

Alternatively, V₂O₅ is emerging as an excellent option for addressing the aforementioned issues by constructing heterostructured binary metal oxides. V₂O₅ is distinguished by its high theoretical C_w of 2,120 F/g, multiple oxidation states (V⁵⁺, V⁴⁺, V³⁺, and V²⁺), cost-effectiveness, excellent chemical stability in electrolyte solutions, and a wide potential window, making it a promising material in this context [36–39]. V₂O₅-based electrodes exhibit superior supercapacitive performance compared with other vanadium oxides, owing to their layered structure and stability [40]. Specifically, the contiguous layers, bonded solely by weak van der Waals forces, significantly contribute to achieving a high energy density through efficient ion

diffusion. Nevertheless, MnO_2 , a pseudocapacitive material, is employed not only to improve the conductivity through composite formation with V_2O_5 but also to enhance the capacitance and reduce the electrode resistance [41,42]. Jia et al. [43] prepared a V_2O_5 nanobelt array–NiO nanosheet array composite, achieving a C_w of 950 F/g at a current density of 1 A/g, showcasing a significantly enhanced performance. Jyothibasu et al. [44] investigated graphite nanoplatelet– V_2O_5 nanotube composite electrodes, attaining a C_w of 420 F/g at a current density of 1 A/g, emphasizing the synergistic effects of the composite material. According to our understanding, there is limited research on MnO_2 – V_2O_5 nanocomposites as electrode materials for emerging supercapacitor applications.

In this research, we investigate the $(MnO_2)_x-(V_2O_5)_{1-x}$ nanocomposites as electrode materials for supercapacitors prepared with different stoichiometric ratios (x = 1, 0.75, 0.50, and 0) using a versatile *ex situ* method to enhance C_w , ionic conductivity, and cyclic stability. In a 1 M KOH aqueous electrolyte, $(MnO_2)_{0.75-}$ $(V_2O_5)_{0.25}$ exhibited a higher C_w of 725 F/g at 5 mV/s, along with a high rate capability with an energy density of 23 Wh/kg. After 1,500 cycles at 0.5 A/g, cycling stability tests showed excellent coulombic efficiency, chemical stability, and 80% capacitance retention rate.

2. Materials and methods

2.1. Materials

All substances were acquired from Sigma Aldrich (United States [US]) and used as received, without any additional refinement or purification. These included ammonium metavanadate (NH₄VO₃), oxalic acid (C₂H₂O₄), potassium permanganate (KMnO₄), manganese sulphate (MnSO₄·4H₂O), polyvinylidene fluoride (PVDF), N-methyl-2-pyrrolidinone (NMP), acetone (C₃H₆O), and carbon black. A sheet of pure 1.6 mm-thick nickel (Ni) foam was sourced from Sigma-Aldrich (China). Chemical solutions were prepared using deionised water (DIW).

2.2. Synthesis of V₂O₅, MnO₂, and their nanocomposites

The synthesis procedures for V_2O_5 , MnO_2 , and $(MnO_2)_x-(V_2O_5)_{1-x}$ nanocomposites (x = 1, 0.75, 0.50, and 0) are explained individually and illustrated schematically in **Figure 1.**

Vanadium pentoxide nanoparticles were fabricated through an easy, straightforward, and cost-effective sol–gel method, in which NH₄VO₃ and C₂H₂O₄ were used as precursors. In this process, the solutions were prepared separately in two different beakers. In beaker "A," 3.580 g of C₂H₂O₄, and in beaker "B," 7.018 g of NH₄VO₃ were each dissolved in 50 mL of DIW. Following preparation, the solution from beaker "A" was added dropwise into beaker B to achieve the desired pH, and then the resulting mixture was stirred at 60°C for 2 h to form a gel. During synthesis, the pH of the solution was adjusted to 12 to promote phase formation and stabilise the V₂O₅ nanoparticles. The prepared gel was dried at 80°C for 24 h, and the resulting powder was repeatedly centrifuged with ethanol and DIW. Subsequently, the product

was ground for 2 h and annealed at 400°C for 4 h in a muffle furnace, yielding yellowish nanoparticles.

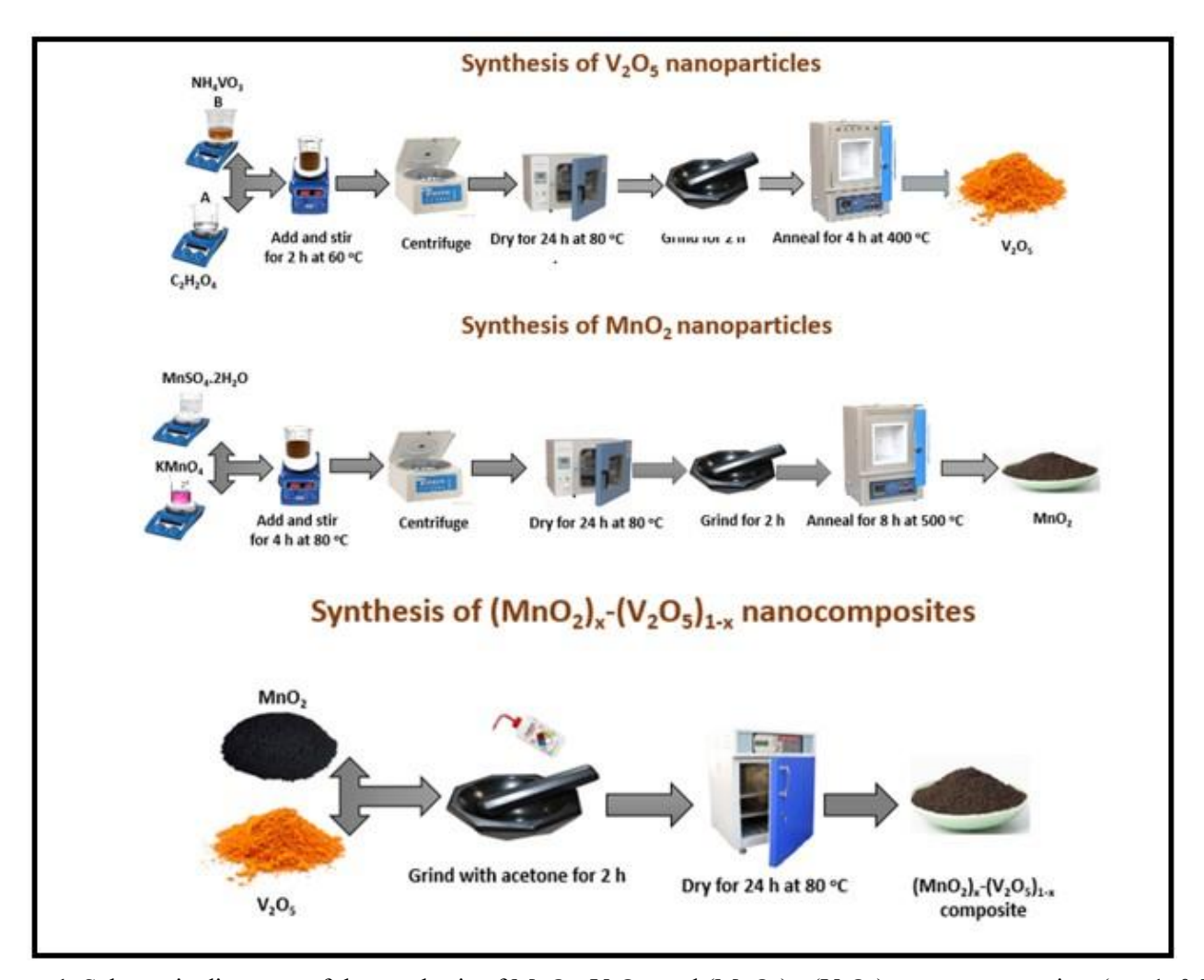


Figure 1. Schematic diagrams of the synthesis of MnO_2 , V_2O_5 , and $(MnO_2)_x$ – $(V_2O_5)_{1-x}$ nanocomposites (x = 1, 0.75, 0.50, and 0).

Similarly, a simple sol–gel method was used to synthesise MnO₂ nanoparticles, using KMnO₄ and MnSO₄·4H₂O as precursors in a 1:2 molar ratio. During this procedure, 2 g of KMnO₄ was dissolved in 60 mL of DIW and stirred at standard room temperature using a magnetic stirrer. Simultaneously, in another beaker, 4 g of MnSO₄·4H₂O was dissolved in 30 mL of DIW. Subsequently, the aqueous KMnO₄ solution was added dropwise into the MnSO₄·4H₂O solution while maintaining the desired pH, and the mixture was stirred for 4 h at 80°C to form a gel. The resulting gel was then centrifuged multiple times with DIW and ethanol to remove impurities. The wet precipitates were dried for 24 h at 80°C in a hot-air oven. After drying, the samples were finely ground and annealed at 500°C for 8 h in a muffle furnace, yielding a light greyish-black MnO2 nanopowder.

The $(MnO_2)_x$ – $(V_2O_5)_{1-x}$ nanocomposites were synthesised via an *ex situ* method using different stoichiometric ratios (x = 1, 0.75, 0.50, and 0) of MnO₂ and V₂O₅. The precursor powders were mixed and ground in a mortar and pestle for 2 h. During the grinding process, acetone was added dropwise 4–5 times to facilitate the formation of

a homogeneous mixture. After fine grinding, the sample was dried in a hot-air oven at 80°C for 24 h to ensure complete evaporation of residual acetone and moisture.

2.3. Characterisation of materials

The crystal structure, crystallite size, and phase identification of the fabricated materials were analysed using X-ray diffraction (XRD), covering a 2θ range from 10° to 70° with a step size of 0.02° . The morphology, average particle size, and elemental composition of the synthesized samples were examined using scanning electron microscopy (SEM) and energy-dispersive X-ray spectroscopy. Fourier transform infrared (FT-IR) spectroscopy was employed to identify the functional groups and molecular vibrations of the samples across the wavenumber range of $4,000-400~\text{cm}^{-1}$, utilising KBr as a reference. The optical bandgap energy (Eg) was determined by UV-visible spectroscopy within the range of 200-800~nm, and further estimated from the Tauc plot relation.

2.4. Fabrication of working electrodes for electrochemical measurements

To analyse the electrochemical performance of the working electrode, Ni foam, used as the electrode substrate, was first activated through sequential washing with 3 M HCl, ethanol, and DIW to remove surface contaminants and impurities, followed by drying overnight at 60°C. Next, the slurry for the working electrode was prepared using the active material, conductive additive, solvent, and binder. In this process, the electrode active material (80%), carbon black (10%), and PVDF (10%) were ground together for 30 min. The resulting mixture was then mixed with 5% NMP and stirred for 12 h to obtain a slurry. The resulting slurry was coated onto a Ni foam electrode (surface area: 1 cm²) to form a thin and uniform layer. Then, the coated electrode was dried in an electric oven at 70°C for 6 h to remove any residual solvent. The average active material loading on the Ni foam surface was approximately 2 mg. The same procedure was followed for all samples.

The supercapacitor device was assembled using two identical electrodes coated with the $(MnO_2)_x$ – $(V_2O_5)_{1-x}$ nanocomposite as the active material. A porous polypropylene membrane served as a separator, placed between the electrodes to allow for ionic transport while preventing electrical shorting. The entire assembly was immersed in an aqueous electrolyte (1 M KOH), as shown in **Figure 2**, and the components were pressed together to ensure good contact. A current collector was used to complete the symmetric supercapacitor cell configuration.

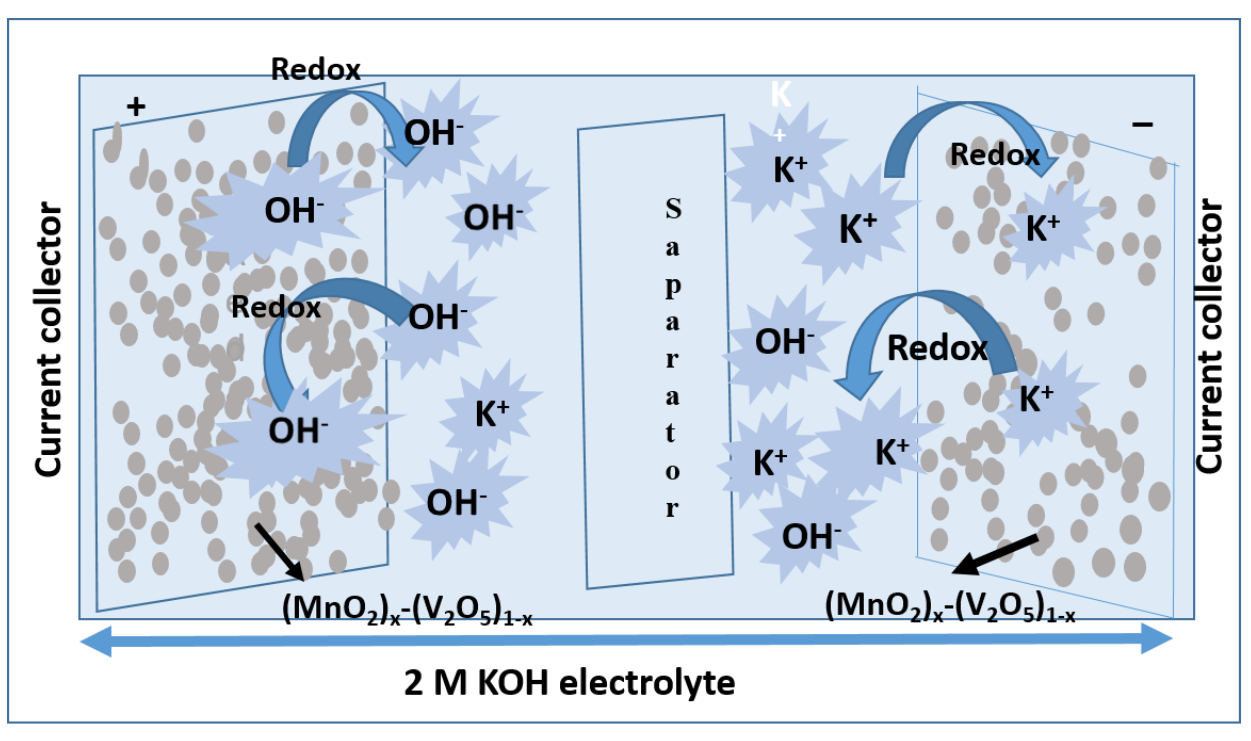


Figure 2. Schematic representation of the supercapacitor assembly and the corresponding charge storage mechanism in the $(MnO_2)_{x-}(V_2O_5)_{1-x}$ nanocomposites.

3. Results and discussion

3.1. Structural analysis

The structural properties and phase formation of MnO₂, V₂O₅, and (MnO₂)_{0.75}– (V₂O₅)_{0.25} electrode materials were analysed using XRD with Cu–K_{α} radiation (a wavelength of 1.5406 Å) as the source. The MnO₂ nanostructures exhibited intense diffraction peaks corresponding to a tetragonal crystal structure [45], observed at 20 angles of 21.8°, 35.1°, 36.9°, 42.1°, 47.7°, 55.4°, 56.9°, 63.1°, and 65.1°, which correspond to the crystal planes (110), (101), (020), (111), (210), (211), (220), (002), and (310), respectively. These reflections are consistent with the standard Joint Committee on Powder Diffraction Standards (JCPDS) card number 81-2261 [46], as presented in **Figure 3**.

Similarly, the V_2O_5 sample displayed characteristic peaks of an orthorhombic structure [47] at 2θ angles of 20° , 21.3° , 26.1° , 30.9° , 32.50° , 34.1° , 41.23° , 45.45° , 47.50° , 48.7° , 51.3° , 55.6° , 60.9° , and 61.9° , corresponding to the crystal planes (001), (101), (110), (301), (011), (310) (002), (411), (600), (021) (020), (012), (321), and (710). These match well with the standard JCPDS card number 41-1426 [48], as depicted in **Figure 3.**

The absence of extra peaks in the nanocomposite indicates the formation of a pure crystalline material without additional phases or impurities [49]. The diffraction pattern of $(MnO_2)_{0.75}$ – $(V_2O_5)_{0.25}$, depicted in **Figure 3**, exhibited a minor shift of diffraction peaks towards lower 2 θ angles, which can be attributed to the formation of structural defects within the crystal lattice [50]. Furthermore, compositional changes

caused by the intercalation of vanadium ions can change the lattice parameters, potentially affecting both electronic conductivity and structural stability. The average crystallite sizes of MnO_2 , V_2O_5 , and $(MnO_2)_{0.75}$ – $(V_2O_5)_{0.25}$ were calculated to be 18.2 nm, 28.1 nm, and 26.3 nm, respectively, using the Scherrer equation. The decrease in the crystallite size of MnO_2 – V_2O_5 was accompanied by an increase in the full width at half maximum of the diffraction peaks, indicating that the incorporation of V_2O_5 disrupts the crystal structure and induces stress/strain. This structural distortion facilitates the creation of additional ion diffusion channels and active sites, thereby enhancing the electrochemical performance of the material [51]. Additional parameters are presented in **Table 1**.

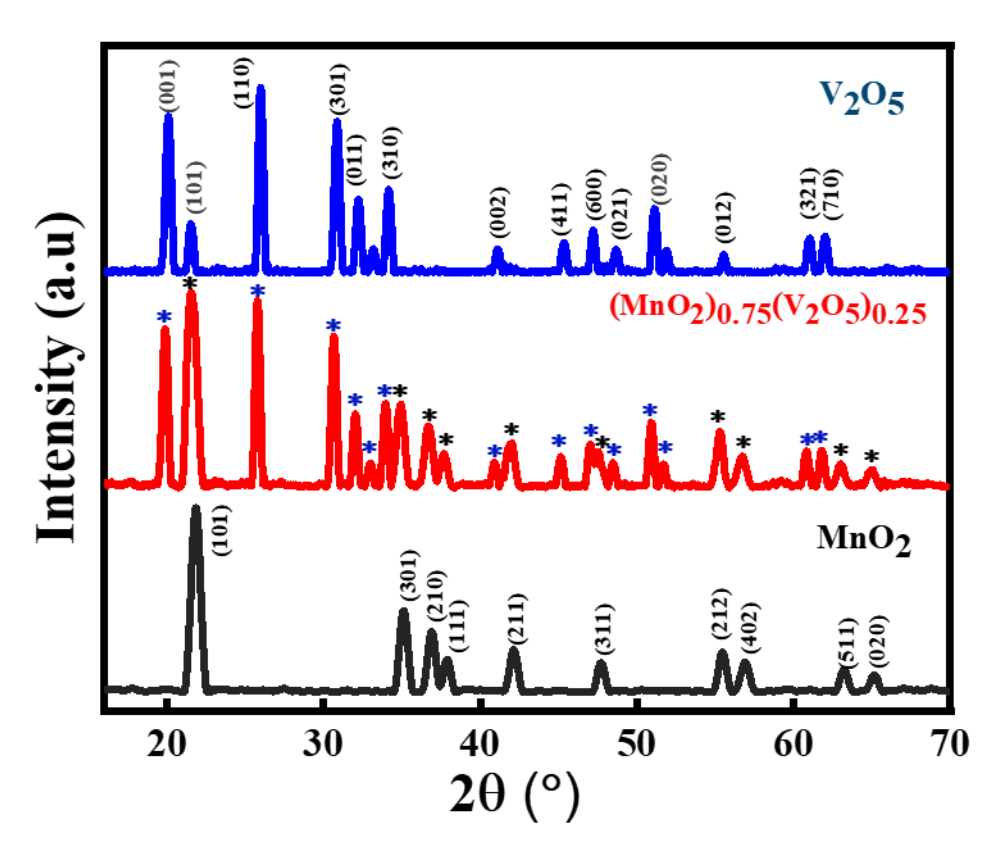


Figure 3. X-ray diffraction pattern of V₂O₅, (MnO₂)_{0.75}–(V₂O₅)_{0.25} nanocomposite, and MnO₂.

Table 1. Parameters of MnO₂, $(MnO_2)0.75-(V_2O_5)0.25$, and V_2O_5 .

| Serial no. | Sample | Peak position (2θ [°]) | FWHM (2θ [°]) | Crystallite size (nm) |
|------------|------------------------------------|---------------------------|------------------|-----------------------|
| 1 | MnO_2 | 65.1 | 0.51 | 18.2 |
| 2 | $(MnO_2)_{0.75} - (V_2O_5)_{0.25}$ | 48.5 | 0.33 | 26.3 |
| 3 | V_2O_5 | 51.8 | 0.31 | 28.1 |

Abbreviation: FWHM: Full width at half maximum.

3.2. Vibrational analysis

Vibrational studies were performed using FT-IR spectroscopy to analyse the functional groups of MnO_2 , V_2O_5 , and $(MnO_2)_x$ – $(V_2O_5)_{1-x}$ nanocomposites, as depicted in **Figure 4**. The absorption bands observed at 524 cm⁻¹, 589 cm⁻¹, and 667 cm⁻¹ corresponded to the vibration modes of the Mn–O bond. The bands at 1,211 cm⁻¹ and 1,365 cm⁻¹ were attributed to the V=O stretching vibrations characteristic of V_2O_5 . Peaks present between 814 cm⁻¹ and 1,001 cm⁻¹ were attributed to the V–O–V stretching vibrations. The absorption peaks at 1,729 cm⁻¹ and 3,407 cm⁻¹ were linked to the O–H stretching and bending vibrations of H_2O molecules, respectively. The main characteristic bands, such as the Mn–O, V=O, and V–O–V bands, in the $(MnO_2)_x$ – $(V_2O_5)_{1-x}$ composites (x=1, 0.75, 0.50, 0) exhibited a slight shift towards lower wavenumbers, indicating chemical bonding interactions between MnO_2 and V_2O_5 phases.

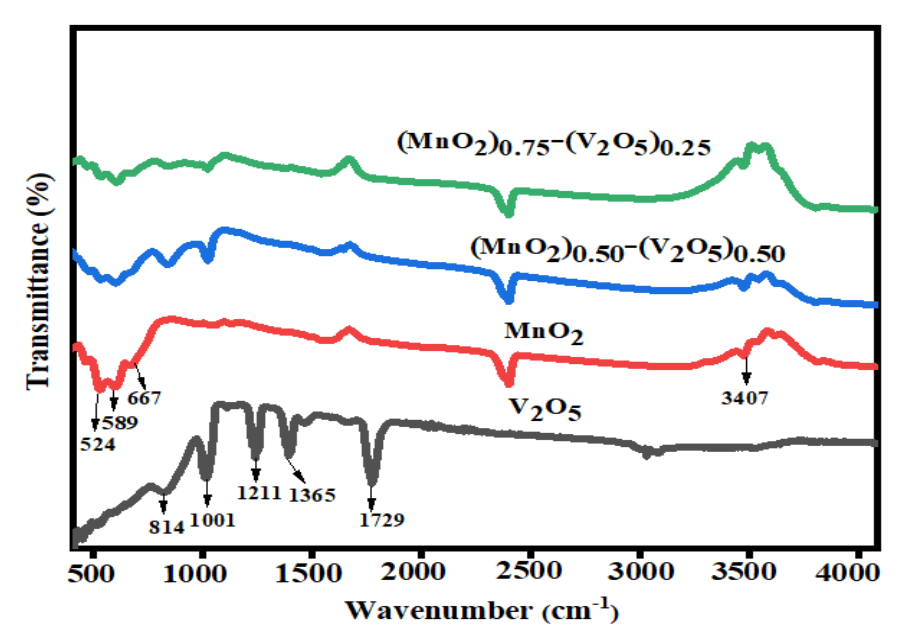


Figure 4. Fourier transform infrared spectra of $(MnO_2)_x$ – $(V_2O_5)_{1-x}$ nanocomposites (x = 1, 0.75, 0.50, and 0).

3.3. Optical analysis

The optical characteristics of MnO_2 , V_2O_5 , and $(MnO_2)_x-(V_2O_5)_{1-x}$ nanocomposites were studied using UV-visible spectroscopy over the wavelength range of 200–800 nm. A significant and extensive absorption peak for MnO_2 was observed at 374 nm, attributed to the d-d transition of Mn ions within the MnO_2 nanostructure (**Figure 5a**). For V_2O_5 , a strong absorption peak appeared at 254 nm, indicating the formation of a single-phase structure (**Figure 5d**). The minor shift towards lower wavelengths in the absorption peaks of the nanocomposites was attributed to the interaction and synergistic effects between the two materials in the nanocomposites, as depicted in **Figure 5b,c**).

The energy band gap of the $(MnO_2)_x$ – $(V_2O_5)_{1-x}$ nanocomposites was determined using the well-defined Tauc's relation:

$$(\alpha h v)^2 = A(h v - E_g)^n \tag{1}$$

where n signifies the nature of the electronic transition (n = 1/2 for indirect transitions and n = 2 for direct transitions), hv is the photon energy, and A is ascribed to absorbance corresponding to the energy band gap (E_g) [52,53]. The computed energy band gap values for MnO₂, (MnO₂)_{0.75}–(V₂O₅)_{0.25}, (MnO₂)_{0.50}–(V₂O₅)_{0.50}, and V₂O₅ were 1.37 eV, 1.40 eV, 1.65 eV, and 2.1 eV, respectively, as depicted in **Figure 5a–d**. The gradual decrease in energy band gap with increasing MnO₂ content demonstrates the semiconducting nature of the nanocomposites and effectively tunes the energy band gap towards the visible region. This narrowing of the band gap facilitates enhanced charge transfer during faradaic redox reactions, thereby improving electrical conductivity and C_w . Through surface redox reactions, MnO₂ contributes to rapid charge storage, whereas V₂O₅ provides more redox-active sites and facilitates electron mobility. Enhanced charge transfer at the interface between the two materials is achieved by their close contact, which reduces internal resistance, enhances conductivity, and improves charge storage behaviour.

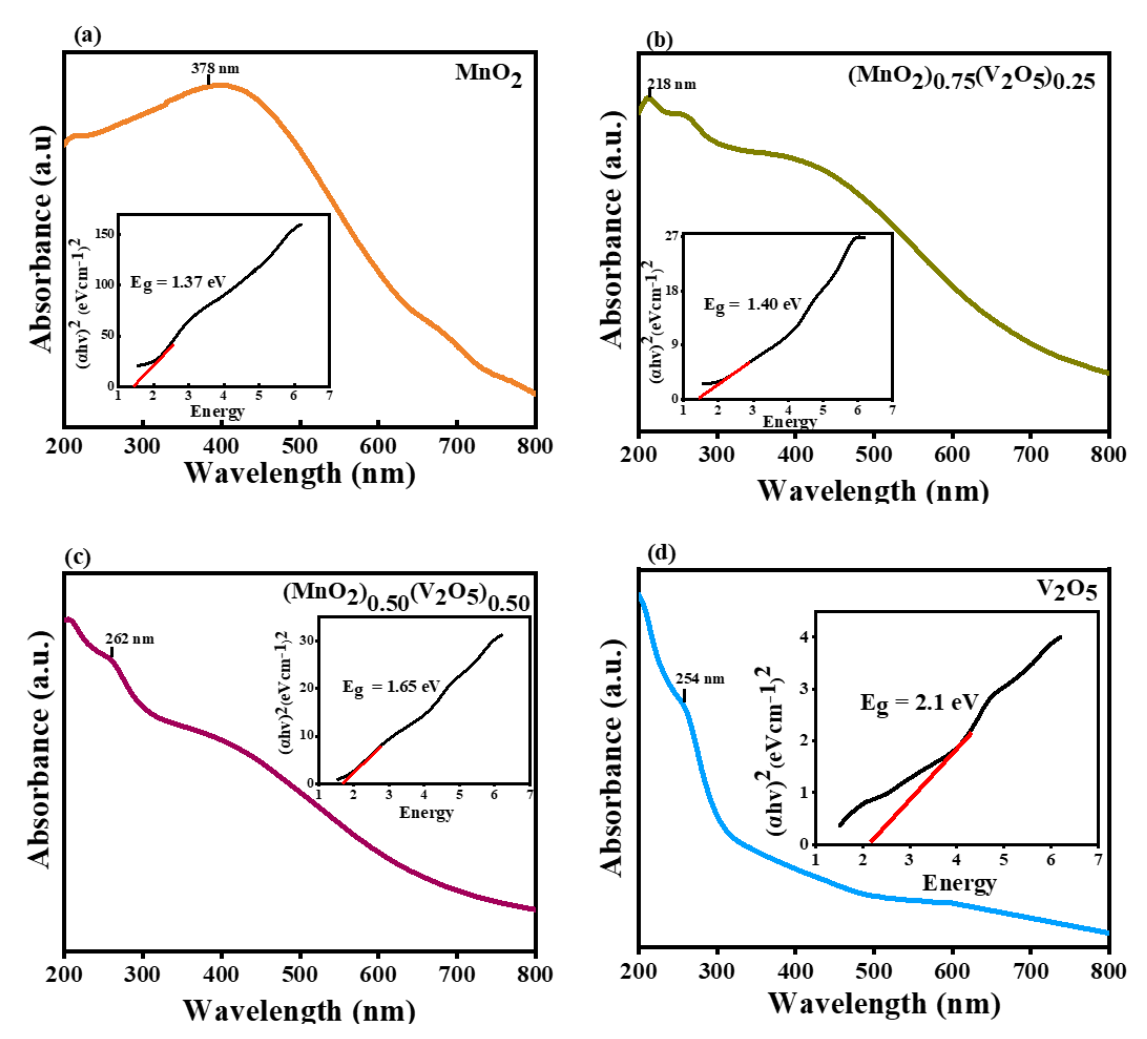


Figure 5. UV-visible absorption spectra and energy band gap of (a) MnO₂, (b) (MnO₂)_{0.75}–(V₂O₅)_{0.25}, (c) (MnO₂)_{0.50}– (V₂O₅)_{0.50}, and (d) V₂O₅.

3.4 Scanning electron microscopy analysis

The surface morphology of synthesised samples—MnO₂, V₂O₅, and (MnO₂)_{0.75}— $(V_2O_5)_{0.25}$ —was examined at various magnifications using SEM, as depicted in **Figure** 6. The nanostructural characteristics were found to be strongly influenced by particle size and distribution. The average particle size, calculated using ImageJ software (National Institutes of Health, US), confirmed the nanoscale nature of the synthesised materials. The SEM micrographs of the nanocomposites revealed that the MnO₂ nanoparticles were adsorbed across the surface of V₂O₅ nanoflakes, as shown in Figure 6d-f. Pure MnO₂ exhibited spherical morphology with discernible agglomeration (Figure 6a-c), which can be attributed to their high surface energy and the natural tendency of unbound nanoparticles to form clusters through strong intermolecular interactions during synthesis and drying. In contrast, pure V₂O₅ exhibited a nanoflake-like structure. In the nanocomposite, the degree of agglomeration was substantially reduced, resulting in a larger effective surface area, improved adsorption capacity, and enhanced charge storage performance. The average particle diameters of $(MnO_2)_x-(V_2O_5)_{1-x}$ (x = 1, 0.75, 0.50, and 0) were in the nanometre range, consistent with XRD results, with minor deviations attributed to particle agglomeration. SEM observations effectively revealed a porous nanoarchitecture, which provides numerous active sites and multiple channels for efficient ion and electron transport—key factors in enhancing faradaic reactions and overall electrochemical performance. Furthermore, EDS analysis confirmed the elemental composition of MnO₂ and (MnO₂)_{0.75}–(V₂O₅)_{0.25} samples. Figure 6g presents elemental mapping of the composite. Mn, V, and O elements were uniformly distributed in the nanocomposite structure.

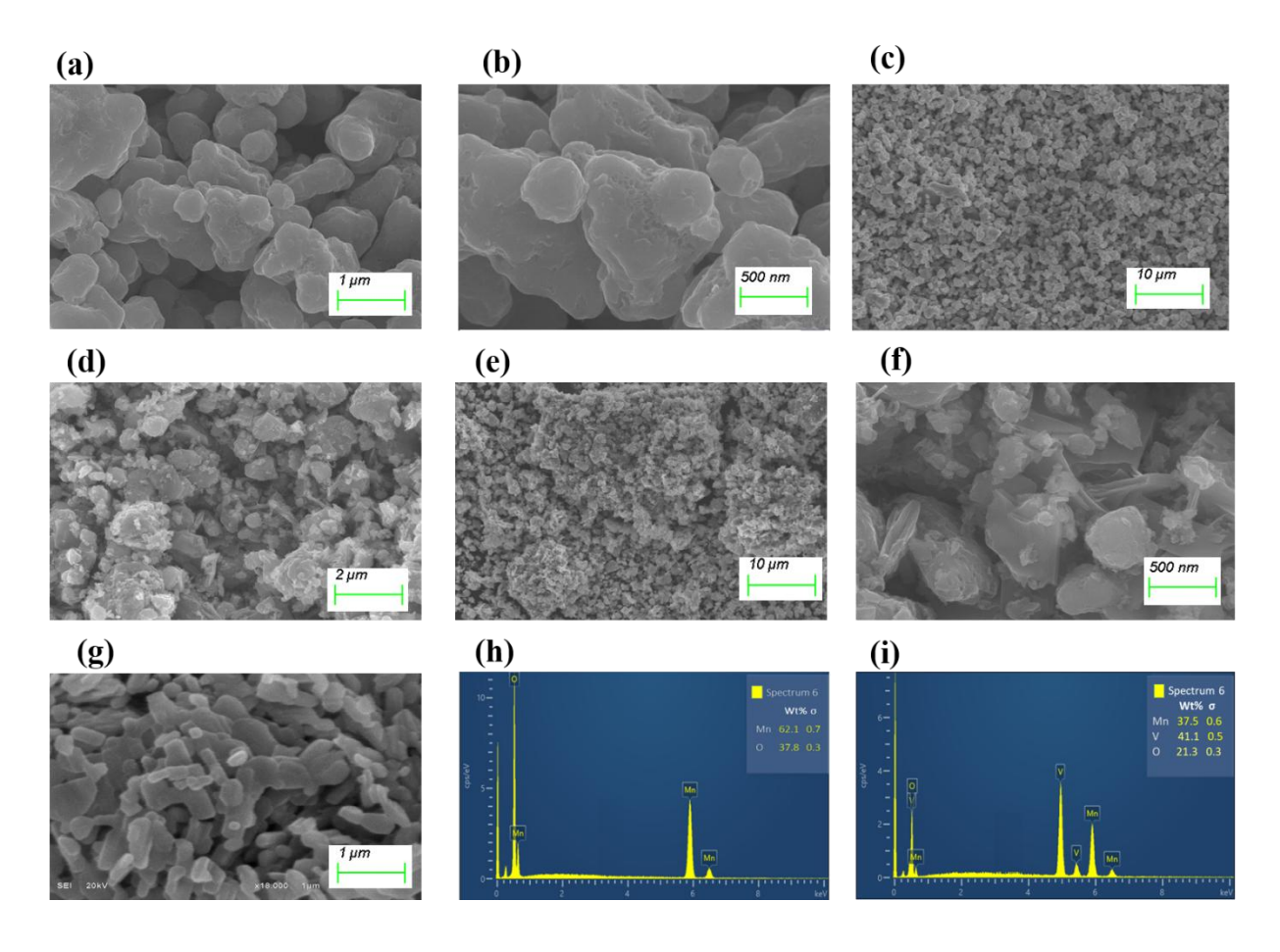


Figure 6. Scanning electron microscopy images of (a–c) MnO₂ nanoparticles, (d–f) (MnO₂)_{0.75}–(V₂O₅)_{0.25}, and (g) V₂O₅ nanoflakes. Scale bars: (a & g) 1 μm, (b & f) 500 nm, (c & e) 10 μm, (d) 2 μm; magnifications: (a & g) 18 000×, (b & f) 20 000×, (c & e) 1000×, (d) 5000×. (h) Energy-dispersive X-ray spectroscopy (EDX) of MnO₂. (i) EDX of (MnO₂)_{0.75}–(V₂O₅)_{0.25}.

3.5 Electrochemical studies

The study of electrochemical properties involves understanding the response and interaction of electrode materials under the influence of electric current and voltage. This aspect is needed for the advancement of batteries, supercapacitors, and various energy storage devices [54]. The electrochemical properties, such as electrical conductivity, charge storage capacity, and electrochemical stability, influence the performance and efficiency of electrochemical devices [55].

All measurements of the fabricated electrodes were tested using an electrochemical workstation (Gamry Interface 1000E potentiostat, Gamry Instruments, US) equipped with a three-electrode system at room temperature. The setup consisted of a counter electrode, an Ag/AgCl reference electrode, and a working electrode (MnO₂-V₂O₅), all of which were immersed in 1 M KOH electrolyte. The abovedescribed procedure (fabrication of working electrode) was repeated for all samples. The electrochemical characteristics of the working electrode were examined through various techniques, such as galvanostatic charge-discharge (GCD) measurements, which were performed at various current densities ranging from 0.5-2 A/g within a potential window of 0-0.5 V to ensure electrochemical stability, show reversible charge-discharge behaviour, and avoid decomposition of electrolyte; cyclic voltammetry, which was conducted at several scan rates (5–100 mV/s) over a potential range of 0-0.6 V to demonstrate the redox behaviour and capacitive response of the electrodes; and electrochemical impedance spectroscopy (EIS), which was carried out with a frequency range of 0.1–100 kHz. Additionally, coulombic efficiency and capacitance retention were analysed over 1,500 cycles.

Cyclic voltammetry was used to examine the electrochemical responses of the prepared MnO_2 , V_2O_5 , and $(MnO_2)_x-(V_2O_5)_{1-x}$ nanocomposites. A cyclic voltammogram reveals the adsorption and desorption of electrolyte ions on the electrode surface, forming an electric double layer known as the Helmholtz layer. Meanwhile, rapid and reversible faradaic redox reactions occur due to ion intercalation at the electrode–electrolyte interface within the TMOs (MnO_2 and V_2O_5). The redox peaks demonstrate the pseudocapacitive nature of the electrode, and the C_w is calculated as follows:

$$C_W = \frac{A}{2mk\Delta V} \tag{2}$$

where m is the mass of active materials, A is the area of the cyclic voltammetric curve, ΔV is the potential window, and k corresponds to the scan rate.

The current response and area under the curve increased progressively with scan rate from 5–100 mV/s in 1 M KOH electrolyte within a potential window of 0–0.6 V (**Figure 7a–d**). The voltammograms exhibited faradic peaks that corresponded to redox reactions and a diffusion-controlled mechanism occurring at the electrode–electrolyte interface during cathodic and anodic sweeps. These peaks were particularly

noticeable at the lower scan rate of 5 mV/s, where electroactive species and electrolyte ions had sufficient time to interact. The trend of C_w is depicted in **Table 2**. As the scan rate increased, the C_w gradually declined, which can be attributed to the limited time for ions to reach the inner active sites of the electrode materials. Additionally, the oxidation peaks shifted towards more positive potentials, whereas the reduction peaks moved towards more negative potentials, indicating the presence of internal resistance within the electrode. Notably, the C_w of (MnO₂)_{0.75}–(V₂O₅)_{0.25} nanocomposite achieved 725 F/g, outperforming the individual electrodes of MnO₂ (230 F/g) and V₂O₅ (553 F/g). This enhancement can be ascribed to the formation of a heterojunction at the MnO₂–V₂O₅ interface, which facilitates efficient interfacial charge transfer. The incorporation of V₂O₅ introduced additional active sites and promoted faster ion diffusion, thereby reducing charge transfer resistance. This effect accelerated faradaic redox reactions and electric double-layer formation, resulting in enhanced overall charge storage capacity. **Figure 7e,f** depicts the comparison of C_w for each sample at varying scan rates.

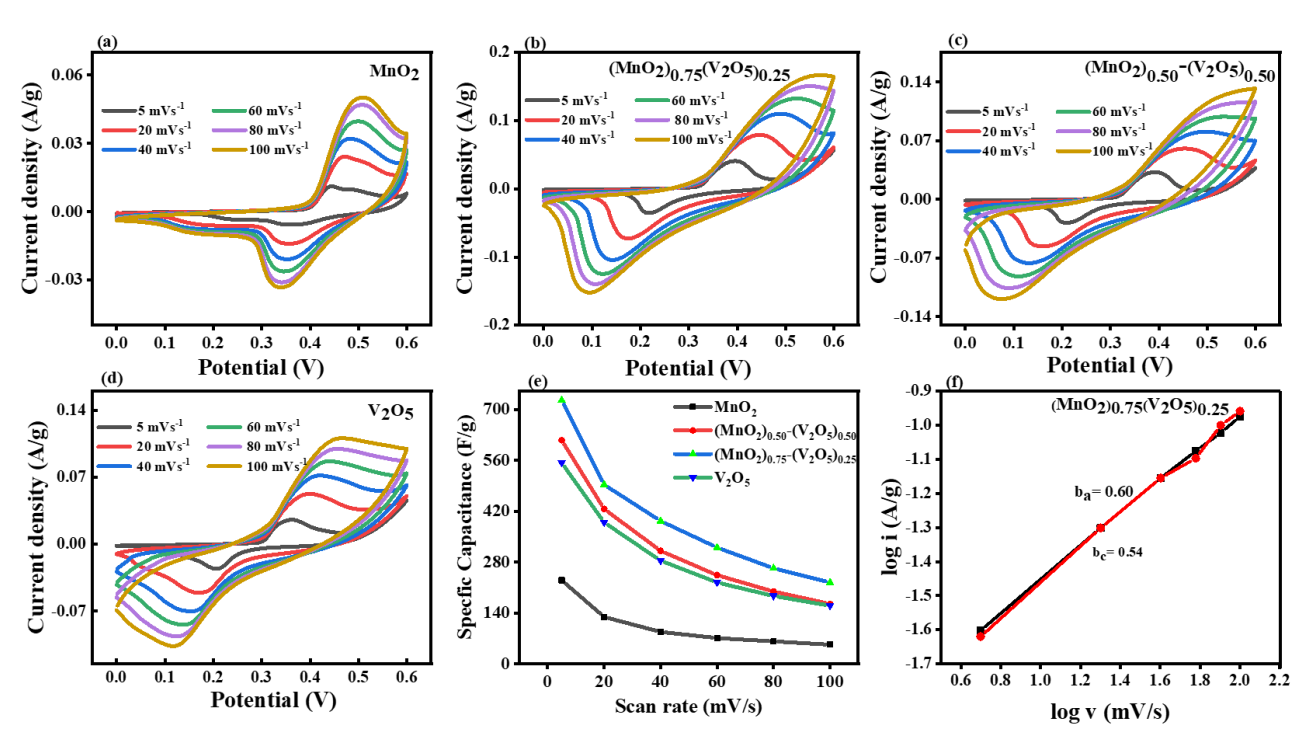


Figure 7. Cycle voltammetry measurements of (a) MnO_2 , (b) $(MnO_2)_{0.75}$ – $(V_2O_5)_{0.25}$, (c) $(MnO_2)_{0.50}$ – $(V_2O_5)_{0.50}$, and (d) V_2O_5 . (e) Specific capacitance vs. scan rate. (f) Reliance of i_c and i_a currents on the sweep rate scan rate.

To further elucidate the charge storage mechanism, b-value analysis was conducted using the power-law relationship:

$$i = av^b (3)$$

where v is the scan rate, i is the peak current, and b indicates the slope obtained from the linear fit. The b value provides insight into the dominant charge storage process: when b = 1, the current response is capacitive-controlled; whereas b = 0.5 corresponds to a charge storage mechanism controlled by ion diffusion. The obtained b value for the cathodic and anodic peaks of the nanocomposite fell between 0.54 and 0.60,

suggesting the K^+ cation storage in $(MnO_2)_{0.75}$ – $(V_2O_5)_{0.25}$, which is a characteristic of pseudocapacitive processes.

| Table 2. Specific capacitance (Cw) of the nanocomp | iposites measured at various scan rates. |
|---|--|
|---|--|

| Serial no. | Materials | C_w (F/g) | | | | | |
|------------|--------------------------------------|-------------|---------|---------|---------|---------|----------|
| | | 5 mV/s | 20 mV/s | 40 mV/s | 60 mV/s | 80 mV/s | 100 mV/s |
| 1 | MnO ₂ | 230 | 129 | 88 | 71 | 62 | 53 |
| 2 | $(MnO_2)_{0.75} - (V_2O_5)_{0.25}$ | 725 | 493 | 393 | 319 | 263 | 223 |
| 3 | $(MnO_2)_{0.50}$ - $(V_2O_5)_{0.50}$ | 615 | 426 | 311 | 244 | 199 | 165 |
| 4 | V_2O_5 | 553 | 389 | 284 | 224 | 187 | 160 |

The charge storage behaviour at the electrode–electrolyte interface was further studied using GCD measurements for MnO₂, V₂O₅, and (MnO₂)_x–(V₂O₅)_{1-x} nanocomposites. The GCD plots for all samples, recorded at current densities of 0.5–2.0 A/g in 1 M KOH electrolyte, are illustrated in **Figure 8a–d**, while the corresponding C_w values are listed in **Table 3**. For each sample, the charge–discharge curve clearly demonstrated the pseudocapacitive behaviour of the materials within a potential window of 0–0.5 V. At the beginning of the discharge cycle, a noticeable voltage drop was observed, which was attributed to the internal resistance of the electrode material. The maximum discharge time was recorded at the lowest current density of 0.5 A/g, as the electrolyte ions have sufficient time to diffuse and interact with the electrode's active sites [56]. Conversely, at higher current densities, the C_w decreased due to insufficient interaction time, resulting in increased kinetic irreversibility of the ions [57]. The C_w was determined from the GCD curve using the following equation:

$$C_w = \frac{I \times \Delta t}{\Delta V \times m} \tag{4}$$

where ΔV is the potential window, I and m represent current density, and Δt is the discharge time. The C_w for MnO₂, (MnO₂)_{0.75}–(V₂O₅)_{0.25}, (MnO₂)_{0.50}–(V₂O₅)_{0.50}, and V₂O₅ were calculated to be 214 F/g, 666 F/g, 607 F/g, and 515 F/g, respectively, at the lowest current density of 0.5 A/g. **Figure 8e,f** illustrates the C_w for each sample at varying current densities. The energy density and power density of the electrochemical supercapacitor were estimated from the GCD plots using the following equations:

$$E = \frac{1}{2}C_w\Delta V^2 \tag{5}$$

$$P = \frac{E}{\Lambda t} \tag{6}$$

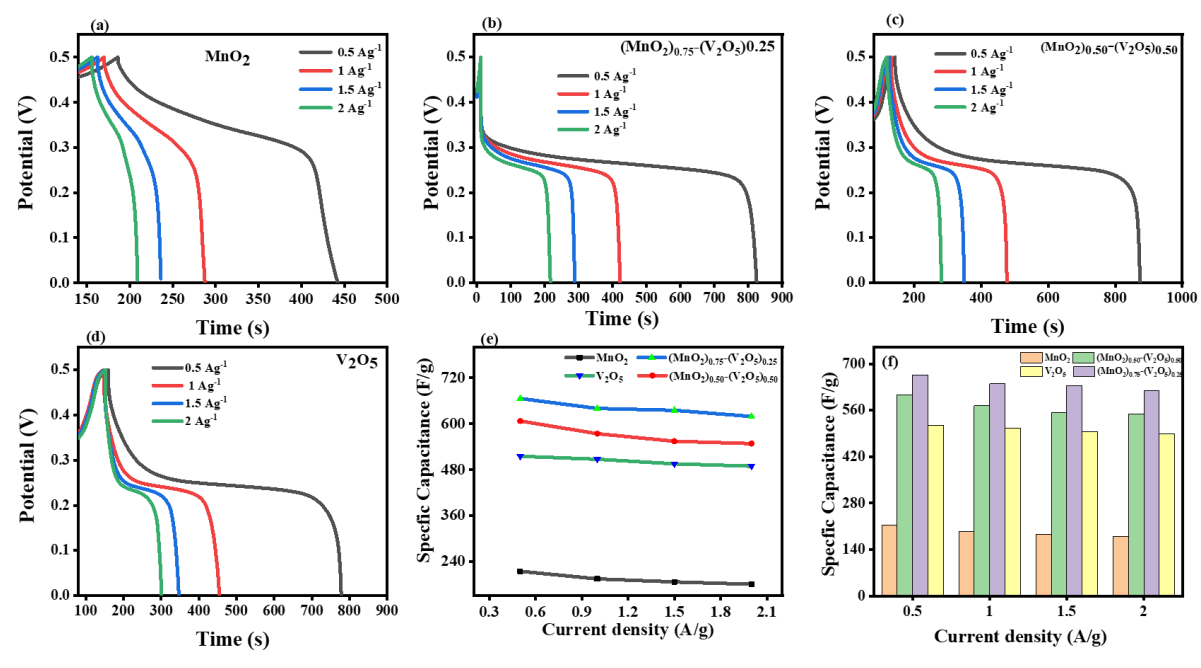


Figure 8. Galvanostatic charge–discharge curves of (a) MnO₂, (b) (MnO₂)_{0.75}–(V₂O₅)_{0.25}, (c) (MnO₂)_{0.50}–(V₂O₅)_{0.50}, and (d) V₂O₅. (e) Specific capacitance vs. current density. (f) Graphical comparison of specific capacitance vs. varying current densities.

The $(MnO_2)_{0.75}$ – $(V_2O_5)_{0.25}$ electrode demonstrated outstanding electrochemical performance at a maximum current density of 2 A/g, with an impressive energy density of 23 Wh/kg and a power density of 450 W/kg. These results aligned with the C_w values measured at numerous scan rates for the $(MnO_2)_x$ – $(V_2O_5)_{1-x}$ (x=0,0.75,0.50, and 1) nanocomposites using cyclic voltammogram.

Table 3. Specific capacitance (Cw) of (MnO₂)x–(V₂O₅)1–x nanocomposites measured at various current densities.

| Serial no. | Materials | C_{w} (F/g) | | | | |
|------------|---|---------------|---------|---------|---------|--|
| | | 0.5 A/g | 1.0 A/g | 1.5 A/g | 2.0 A/g | |
| 1 | MnO ₂ | 214 | 194 | 186 | 180 | |
| 2 | (MnO ₂) _{0.75} –(V ₂ O ₅) _{0.25} | 666 | 640 | 635 | 619 | |
| 3 | (MnO ₂) _{0.50} -(V ₂ O ₅) _{0.50} | 607 | 574 | 554 | 548 | |
| 4 | V_2O_5 | 515 | 507 | 495 | 489 | |

The measurements of EIS were obtained to analyse the charge transfer properties of the electrode–electrolyte interface of the nanocomposites. In the Nyquist plot, the real component (Z'), plotted along the x-axis, represents the ohmic characteristics, whereas the imaginary component (Z"), plotted on the y-axis, denotes the capacitive or inductive properties of the electrochemical cell [58]. The smaller semi-circle observed for the $(MnO_2)_{0.75}$ – $(V_2O_5)_{0.25}$ electrode indicates a notably lower charge transfer resistance. Additionally, the Nyquist plot of the $(MnO_2)_{0.75}$ – $(V_2O_5)_{0.25}$ electrode was fitted with an equivalent circuit model, wherein the alternating current

signal passes through the solution resistance connected in series across all frequencies, as shown in **Figure 9e.** The solution resistance values for $(MnO_2)_x$ – $(V_2O_5)_{1-x}$ (x=1, 0.75, 0.50, and 0) were determined as 0.51 Ω , 0.24 Ω , 0.44 Ω , and 0.84 Ω , respectively, as represented in **Figure 9a–d.** The irregularity of the electrode surface and the reduced pore size contributed to increased solution resistance and electrolyte ion resistance. At lower frequencies, the linear response reflects the diffusion of electrolyte ions at the electrode surface, contributing to considerable resistance. The combined electrochemical activities of V_2O_5 and MnO_2 accounted for this remarkable performance. Both pseudocapacitive metal oxides were distinguished by their high redox activity and stability.

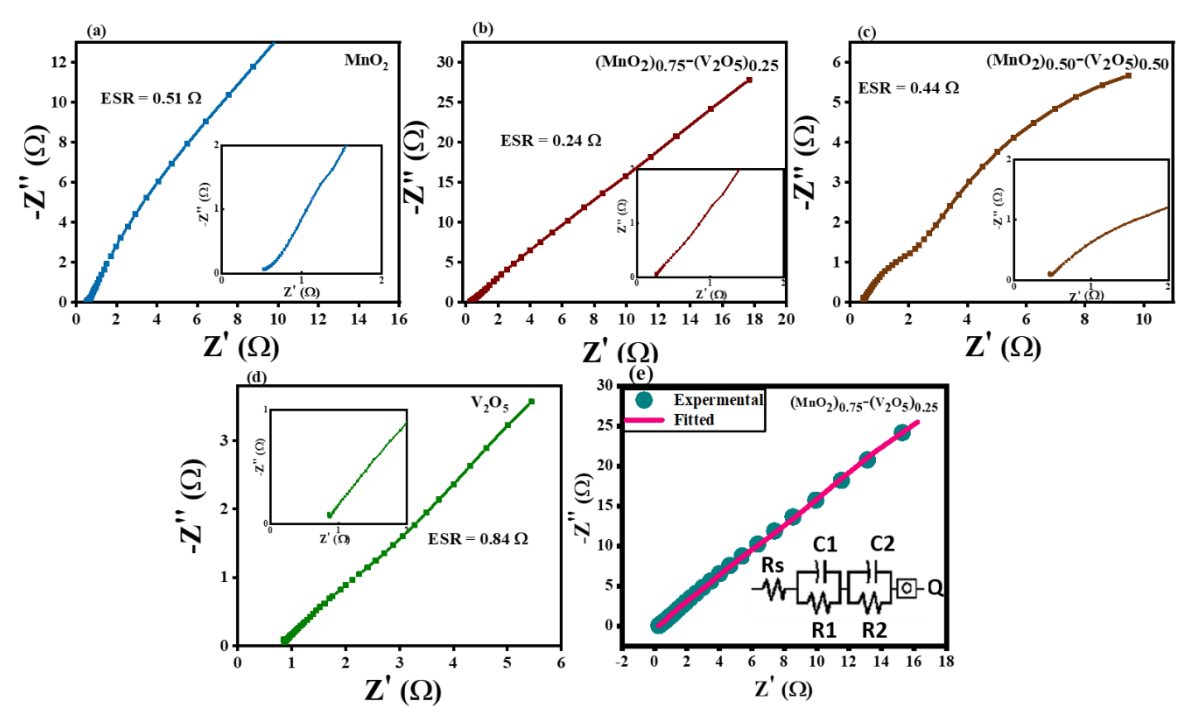


Figure 9. Nyquist plots of (a) MnO₂, (b) (MnO₂)_{0.75}–(V₂O₅)_{0.25}, (c) (MnO₂)_{0.50}–(V₂O₅)_{0.50}, and (d) V₂O₅. (e) Fitted Nyquist plot with an equivalent circuit. Abbreviation: ESR: Equivalent series resistance.

The cyclic stability of MnO₂, V₂O₅, and (MnO₂)_x—(V₂O₅)_{1-x} nanocomposites was evaluated using GCD testing over 1,500 cycles at 0.5 A/g to assess the behaviour of the working electrodes. As shown in **Figure 10**, the (MnO₂)_{0.75}—(V₂O₅)_{0.25} electrode achieved a capacitance retention of 95% and an outstanding coulombic efficiency of 98%, demonstrating excellent stability compared to the capacitance retention of the individual MnO₂ (74%) and V₂O₅ (80%). The increased cyclic stability of the nanocomposite electrode can be attributed to the incorporation of V₂O₅, which not only improves the conductivity but also increases capacity and stabilises the MnO₂ nanostructure. In contrast, when the GCD process was carried out over several cycles in TMOs (MnO₂ and V₂O₅), redox reactions at the electrode—electrolyte interface can slowly disrupt the contact between conductive particles within the composite. This instability may lead to the steady dissolution of Mn and V ions into the electrolyte,

resulting in inactive material degradation, structural instability, and reduced electrochemical performance over time. Overall, the enhancement in stability implies enhanced structural integrity, reduced degradation rate, and consistent electrochemical performance, confirming the potential of the nanocomposite electrode in energy storage applications [59].

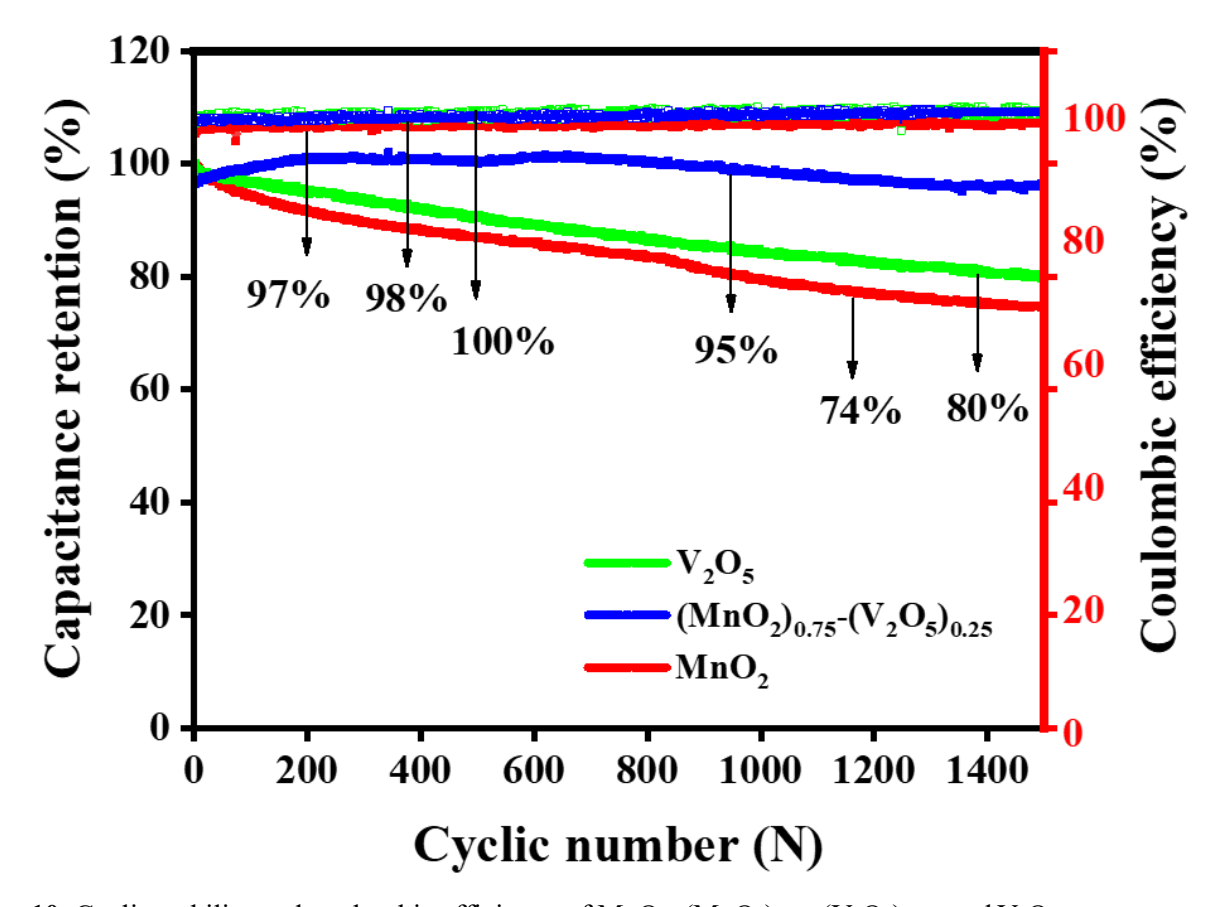


Figure 10. Cyclic stability and coulombic efficiency of MnO₂, (MnO₂)_{0.75}–(V₂O₅)_{0.25}, and V₂O₅ nanocomposite.

4. Conclusion

In conclusion, we successfully fabricated $(MnO_2)_x-(V_2O_5)_{1-x}$ (x = 1, 0.75, 0.50, and 0) nanocomposites as electrode materials for supercapacitor applications through a simple chemical method. XRD studies confirmed the phase purity and crystalline structure of all samples, while SEM and EDS mapping verified their morphology. UV-visible spectroscopy revealed that the energy band gap of the nanocomposite shifted towards the visible region due to defect sites present in the crystal structure. Electrochemical studies demonstrated that the $(MnO_2)_{0.75}-(V_2O_5)_{0.25}$ nanocomposite electrode showed outstanding electrochemical performance, achieving a C_w of 666 F/g at a current density of 0.5 A/g, with a low resistance $(0.24 \,\Omega)$, excellent cyclic stability (95%), and high coulombic efficiency (98%) after 1,500 cycles. Moreover, the energy density (23 Wh/kg) and power density (450 W/kg) for the $(MnO_2)_{0.75}-(V_2O_5)_{0.25}$ nanocomposite were enhanced due to the synergistic effect of MnO₂ and V_2O_5 . Overall, the advancement of TMO-based nanocomposites highlights their potential use for

efficient energy storage. Furthermore, the nanocomposite electrode exhibited significant energy density and consistent electrochemical characteristics, suggesting the nanocomposite is a promising material for supercapacitors.

Author contributions: Conceptualization, Javed Iqbal; visualization, Sobia Jabeen; writing—original draft, Amna Khalid; writing—review and editing, Sobia Jabeen. All authors have read and agreed to the published version of the manuscript.

Acknowledgments: The authors would like to express their sincere gratitude to their supervisor, Prof. Javed Iqbal, for his valuable guidance and support throughout this research. The authors acknowledge the Department of Physics, LNT Laboratory, and Quaid-i-Azam University, Islamabad, Pakistan, for providing the necessary research facilities. Appreciation is also extended to all the institutes affiliated with the authors of this manuscript for their cooperation and assistance.

Data availability statement: The data supporting the findings of this study are available upon request.

Conflict of interest: The authors declare no conflict of interest.

References

- 1. Strielkowski W, Civín L, Tarkhanova E, et al. Renewable Energy in the Sustainable Development of Electrical Power Sector: A Review. Energies. 2021; 14(24): 8240. doi: 10.3390/en14248240
- 2. Gielen D, Boshell F, Saygin D, et al. The role of renewable energy in the global energy transformation. Energy Strategy Reviews. 2019; 24: 38-50. doi: 10.1016/j.esr.2019.01.006
- 3. Kalyani NT, Dhoble SJ. Energy materials: Applications and propelling opportunities. Energy Materials. Published online 2021: 567-580. doi: 10.1016/b978-0-12-823710-6.00011-x
- 4. Ohsaki, T., et al., High performance thin lithium-ion battery using an aluminum-plastic laminated film bag, in Studies in Surface Science and Catalysis. 2001, Elsevier. p. 925-928. https://doi.org/10.1016/S0167-2991(01)82238-2 https://doi.org/10.1016/S0167-2991(01)82238-2
- 5. Shafiullah M, Refat AM, Haque ME, et al. Review of Recent Developments in Microgrid Energy Management Strategies. Sustainability. 2022; 14(22): 14794. doi: 10.3390/su142214794
- 6. Raza W, Ali F, Raza N, et al. Recent advancements in supercapacitor technology. Nano Energy. 2018; 52: 441-473. doi: 10.1016/j.nanoen.2018.08.013
- 7. Khedulkar AP, Dang VD, Thamilselvan A, et al. Sustainable high-energy supercapacitors: Metal oxide-agricultural waste biochar composites paving the way for a greener future. Journal of Energy Storage. 2024; 77: 109723. doi: 10.1016/j.est.2023.109723
- 8. Pathak M, Bhatt D, Bhatt RC, et al. High Energy Density Supercapacitors: An Overview of Efficient Electrode Materials, Electrolytes, Design, and Fabrication. The Chemical Record. 2023; 24(1). doi: 10.1002/tcr.202300236
- 9. Huang S, Zhu X, Sarkar S, et al. Challenges and opportunities for supercapacitors. APL Materials. 2019; 7(10). doi: 10.1063/1.5116146
- 10. Forouzandeh P, Kumaravel V, Pillai SC. Electrode Materials for Supercapacitors: A Review of Recent Advances. Catalysts. 2020; 10(9): 969. doi: 10.3390/catal10090969
- 11. Vadivel S, Hariganesh S, Paul B, et al. Bismuth Enriched Materials for Pseudo Capacitor Applications. Encyclopedia of Energy Storage. Published online 2022: 581-589. doi: 10.1016/b978-0-12-819723-3.00039-1
- 12. Zhang G, Xiao X, Li B, et al. Transition metal oxides with one-dimensional/one-dimensional-analogue nanostructures for advanced supercapacitors. Journal of Materials Chemistry A. 2017; 5(18): 8155-8186. doi: 10.1039/c7ta02454a
- 13. Tatrari G, Ahmed M, Shah FU. Synthesis, thermoelectric and energy storage performance of transition metal oxides composites. Coordination Chemistry Reviews. 2024; 498: 215470. doi: 10.1016/j.ccr.2023.215470

- 14. Dubal DP, Jayaramulu K, Sunil J, et al. Metal Organic Framework (MOF) Derived Electrodes with Robust and Fast Lithium Storage for Li Ion Hybrid Capacitors. Advanced Functional Materials. 2019; 29(19). doi: 10.1002/adfm.201900532
- 15. Kebabsa L, Kim J, Lee D, et al. Highly porous cobalt oxide-decorated carbon nanofibers fabricated from starch as free-standing electrodes for supercapacitors. Applied Surface Science. 2020; 511: 145313. doi: 10.1016/j.apsusc.2020.145313
- 16. Wolf S, Roschger M, Genorio B, et al. Mixed Transition-Metal Oxides on Reduced Graphene Oxide as a Selective Catalyst for Alkaline Oxygen Reduction. ACS Omega. 2023; 8(12): 11536-11543. doi: 10.1021/acsomega.3c00615
- 17. Shaheen I, Hussain I, Zahra T, et al. Recent advancements in metal oxides for energy storage materials: Design, classification, and electrodes configuration of supercapacitor. Journal of Energy Storage. 2023; 72: 108719. doi: 10.1016/j.est.2023.108719
- 18. Goswami M, Kumar S, Siddiqui H, et al. Hybrid energy storage devices: Li-ion and Na-ion capacitors. Emerging Trends in Energy Storage Systems and Industrial Applications. Published online 2023: 223-258. doi: 10.1016/b978-0-323-90521-3.00016-8
- 19. Kumar A, Rathore HK, Sarkar D, et al. Nanoarchitectured transition metal oxides and their composites for supercapacitors. Electrochemical Science Advances. 2021; 2(6). doi: 10.1002/elsa.202100187
- 20. Cao Y, He Y, Gang H, et al. Stability study of transition metal oxide electrode materials. Journal of Power Sources. 2023; 560: 232710. doi: 10.1016/j.jpowsour.2023.232710
- 21. Barbieri O, Hahn M, Foelske A, et al. Effect of Electronic Resistance and Water Content on the Performance of RuO[sub 2] for Supercapacitors. Journal of The Electrochemical Society. 2006; 153(11): A2049. doi: 10.1149/1.2338633
- 22. Revathi P, Krishnasamy K. A facile synthesis of RGO/HfO2 nanocomposite for high-performance supercapacitor. Materials Today: Proceedings. 2021; 47: 1-7. doi: 10.1016/j.matpr.2021.03.460
- 23. Nithya VD, Arul NS. Review on α-Fe2O3 based negative electrode for high performance supercapacitors. Journal of Power Sources. 2016; 327: 297-318. doi: 10.1016/j.jpowsour.2016.07.033
- 24. Jabeen S, Iqbal J, Samarin S, et al. Electrochemical characterization and structural analysis of (In2O3)/(Fe2O3) nanocomposites for high-performance supercapacitors. Ceramics International. 2024; 50(9): 16228-16240. doi: 10.1016/j.ceramint.2024.02.103
- 25. Majumdar D, Mandal M, Bhattacharya SK. V2O5 and its Carbon Based Nanocomposites for Supercapacitor Applications. ChemElectroChem. 2019; 6(6): 1623-1648. doi: 10.1002/celc.201801761
- 26. Yao S, Qu F, Wang G, et al. Facile hydrothermal synthesis of WO3 nanorods for photocatalysts and supercapacitors. Journal of Alloys and Compounds. 2017; 724: 695-702. doi: 10.1016/j.jallcom.2017.07.123
- 27. Gopika. S, Shyju. S. Performance Evaluation of Symmetric Supercapacitors based on Pelletized MnO2 and MnO2 doped V2O5 Electrodes. 2020 4th International Conference on Electronics, Communication and Aerospace Technology (ICECA). Published online November 5, 2020: 281-288. doi: 10.1109/iceca49313.2020.9297616
- 28. Khawula TNY, Raju K, Franklyn PJ, et al. Symmetric pseudocapacitors based on molybdenum disulfide (MoS2)-modified carbon nanospheres: correlating physicochemistry and synergistic interaction on energy storage. Journal of Materials Chemistry A. 2016; 4(17): 6411-6425. doi: 10.1039/c6ta00114a
- 29. P. MS, Vishal JK, Chandra Bose A. Graphene oxide-MnO2 nanocomposite for supercapacitor application. Razeghi M, Ghazinejad M, Bayram C, Yu JS, eds. Carbon Nanotubes, Graphene, and Emerging 2D Materials for Electronic and Photonic Devices IX. 2016; 9932: 99320I. doi: 10.1117/12.2237578
- 30. Patil PH, Jadhav SA. Manganese dioxide (MnO2) and biomass-derived carbon-based electroactive composite materials for supercapacitor applications. RSC Applied Interfaces. 2024; 1(4): 624-647. doi: 10.1039/d4lf00085d
- 31. Zhao W, Rubio SJB, Dang Y, et al. Green Electrochemical Energy Storage Devices Based on Sustainable Manganese Dioxides. ACS ES&T Engineering. 2021; 2(1): 20-42. doi: 10.1021/acsestengg.1c00317
- 32. Gao M. Synthesis of Manganese-Based Electrode Materials Prepared by a Novel Dynamic Floating Electrodeposition (DFE) Method for Energy Storage Devices. Published online 2017. doi: 10.7939/R3S46HJ6X
- 33. Wu D, Xie X, Zhang Y, et al. MnO2/Carbon Composites for Supercapacitor: Synthesis and Electrochemical Performance. Frontiers in Materials. 2020; 7. doi: 10.3389/fmats.2020.00002
- 34. Tatrari G, Tewari C, Pathak M, et al. 3D-graphene hydrogel and tungsten trioxide-MnO2 composite for ultra-high-capacity asymmetric supercapacitors: A comparative study. Journal of Energy Storage. 2023; 68: 107830. doi: 10.1016/j.est.2023.107830
- 35. Shen H, Kong X, Zhang P, et al. In-situ hydrothermal synthesis of δ-MnO2/soybean pod carbon and its high performance application on supercapacitor. Journal of Alloys and Compounds. 2021; 853: 157357. doi: 10.1016/j.jallcom.2020.157357

- 36. Yan Y, Li B, Guo W, et al. Vanadium based materials as electrode materials for high performance supercapacitors. Journal of Power Sources. 2016; 329: 148-169. doi: 10.1016/j.jpowsour.2016.08.039
- 37. Alcántara R, Lavela P, Edström K, et al. Metal-Ion Intercalation Mechanisms in Vanadium Pentoxide and Its New Perspectives. Nanomaterials. 2023; 13(24): 3149. doi: 10.3390/nano13243149
- 38. Yang G, Li Q, Ma K, et al. The degradation mechanism of vanadium oxide-based aqueous zinc-ion batteries. Journal of Materials Chemistry A. 2020; 8(16): 8084-8095. doi: 10.1039/d0ta00615g
- 39. Delbari SA, Ghadimi LS, Hadi R, et al. Transition metal oxide-based electrode materials for flexible supercapacitors: A review. Journal of Alloys and Compounds. 2021; 857: 158281. doi: 10.1016/j.jallcom.2020.158281
- 40. Temam AG, Alshoaibi A, Getaneh SA, et al. Recent progress on V2O5 based electroactive materials: Synthesis, properties, and supercapacitor application. Current Opinion in Electrochemistry. 2023; 38: 101239. doi: 10.1016/j.coelec.2023.101239
- 41. Ran F, Hu M, Deng S, et al. Designing transition metal-based porous architectures for supercapacitor electrodes: a review. RSC Advances. 2024; 14(16): 11482-11512. doi: 10.1039/d4ra01320d
- 42. Xu Y, Yu S, Johnson HM, et al. Recent progress in electrode materials for micro-supercapacitors. iScience. 2024; 27(2): 108786. doi: 10.1016/j.isci.2024.108786
- 43. Jia D, Zheng F, Niu Y, et al. Preparation of V2O5 nanobelt arrays/NiO nanosheet arrays composite as supercapacitor electrode material. Journal of Alloys and Compounds. 2023; 969: 172283. doi: 10.1016/j.jallcom.2023.172283
- 44. Jyothibasu J, Chen MZ, Tien YC, et al. V2O5/Carbon Nanotube/Polypyrrole Based Freestanding Negative Electrodes for High-Performance Supercapacitors. Catalysts. 2021; 11(8): 980. doi: 10.3390/catal11080980
- 45. Devaraj S, Munichandraiah N. Effect of Crystallographic Structure of MnO2 on Its Electrochemical Capacitance Properties. The Journal of Physical Chemistry C. 2008; 112(11): 4406-4417. doi: 10.1021/jp7108785
- 46. Jia J, Yang W, Zhang P, et al. Facile synthesis of Fe-modified manganese oxide with high content of oxygen vacancies for efficient airborne ozone destruction. Applied Catalysis A: General. 2017; 546: 79-86. doi: 10.1016/j.apcata.2017.08.013
- 47. Filonenko VP, Sundberg M, Werner PE, et al. Structure of a high-pressure phase of vanadium pentoxide, β-V2O5. Acta Crystallographica Section B Structural Science. 2004; 60(4): 375-381. doi: 10.1107/s0108768104012881
- 48. Rosyara YR, Pathak I, Muthurasu A, et al. Anion-modulated bifunctional electrocatalytic activity of nickel telluride/cobalt telluride mesoporous nanosheets for high-efficiency and stable overall water splitting. Journal of Materials Chemistry A. Published online 2025. doi: 10.1039/d5ta03463a
- 49. Nabavi M, Sanchez C, Livage J. Structure and properties of amorphous V2O5. Philosophical Magazine B. 1991; 63(4): 941-953. doi: 10.1080/13642819108205549
- 50. Das AS, Dipankar Biswas, Roy M, et al. Effect of V2O5 concentration on the structural and optical properties and DC electrical conductivity of ternary semiconducting glassy nanocomposites. Journal of Physics and Chemistry of Solids. 2019; 124: 44-53. doi: 10.1016/j.jpcs.2018.08.026
- 51. Shireesha K, Chidurala SC. Impact of hybridization on specific capacitance in hybrid NiO/V2O5@graphene composites as advanced supercapacitor electrode materials. Applied Surface Science Advances. 2022; 12: 100329. doi: 10.1016/j.apsadv.2022.100329
- 52. Abdullah O, Tahir D, Saber D. Optical Properties of the Synthesized Cr2S3 Nanoparticles Embedded in Polyvinyl Alcohol. Aro, The Scientific Journal of Koya University. 2015; 3(1): 45-49. doi: 10.14500/aro.10067
- 53. Taranu BO, Novaconi SD, Ivanovici M, et al. α-MnO2 Nanowire Structure Obtained at Low Temperature with Aspects in Environmental Remediation and Sustainable Energy Applications. Applied Sciences. 2022; 12(13): 6821. doi: 10.3390/app12136821
- 54. Wang Y, Song Y, Xia Y. Electrochemical capacitors: mechanism, materials, systems, characterization and applications. Chemical Society Reviews. 2016; 45(21): 5925-5950. doi: 10.1039/c5cs00580a
- 55. Sharma S, Chand P. Supercapacitor and electrochemical techniques: A brief review. Results in Chemistry. 2023; 5: 100885. doi: 10.1016/j.rechem.2023.100885
- Decaux C, Matei Ghimbeu C, Dahbi M, et al. Influence of electrolyte ion—solvent interactions on the performances of supercapacitors porous carbon electrodes. Journal of Power Sources. 2014; 263: 130-140. doi: 10.1016/j.jpowsour.2014.04.024
- 57. Dong R, Ye Q, Kuang L, et al. Enhanced Supercapacitor Performance of Mn3O4 Nanocrystals by Doping Transition-Metal Ions. ACS Applied Materials & Interfaces. 2013; 5(19): 9508-9516. doi: 10.1021/am402257y

- 58. Dhillon S, Kant R. Theory for electrochemical impedance spectroscopy of heterogeneous electrode with distributed capacitance and charge transfer resistance. Journal of Chemical Sciences. 2017; 129(8): 1277-1292. doi: 10.1007/s12039-017-1335-x
- 59. Vinodhini SP, Xavier JR. Electrochemical evaluation and structural characterization of polythiophene surfaces modified with PbO/PbS for energy storage applications. Materials Chemistry and Physics. 2024; 318: 129233. doi: 10.1016/j.matchemphys.2024.129233